Paleoproterozoic oxygenated oceans following the Lomagundi-Jatuli Event

Kaarel Mänd, Stefan V. Lalonde, Leslie J. Robbins, Marie Thoby, Kärt Paiste, Timmu Kreitsmann, Päärn Paiste, Christopher T. Reinhard, Alexander E. Romashkin, Noah J. Planavsky, Kalle Kirsimäe, Aivo Lepland, Kurt O. Konhauser

Supplementary information

Geological setting

The Zaonega Formation (ZF) is part of the Paleoproterozoic volcano-sedimentary succession of the Onega Basin in Karelia, northwestern Russia (Figure S1). It formed on the rifted margin of the Karelian craton in the Svecofennian Ocean and lies unconformably on Archean granites and gneisses[1,2]. The basin underwent regional greenschist facies metamorphism during the 1890–1790 Ma Svecofennian orogeny[1]. The ZF lies above the Tulomozero Formation, a shallow water ^{13}C-enriched carbonate and evaporite succession that records oxygenated seawater conditions[3,4], and is overlain by the basalts of the Suisari Formation[1].

The ZF itself consists of a 1500 m-thick succession of graded greywackes, organic-rich mudstones, and carbonates interbedded and intersected by lava flows, tuff layers, and gabbro intrusions[1,5]. Sedimentation occurred in a rift basin of mixed shallow- and deep-water conditions and was punctuated by abundant turbidity current deposits[5–7]. Synsedimentary volcanic activity—exemplified by peperite contacts of mafic intrusions into unconsolidated, wet sediments—resulted in localized contact metamorphism and initiated hydrocarbon generation and

migration[2,8,9]. The associated high nutrient flux fuelled an exceptionally productive microbial ecosystem that produced one of the oldest phosphorites and one of the largest Paleoproterozoic organic carbon deposits[8,10]. While organic matter in most of the ZF has $\delta^{13}C$ values of ~−25‰ that are characteristic of CO_2 fixation, a section of the middle-to-upper ZF displays $\delta^{13}C_{org}$ values between −25‰ and −40‰, indicative of biomass contribution from methanotrophy[9,11]. Distinctly positive $\delta^{34}S$ values of pyrite in the upper ZF have been interpreted as resulting from high microbial sulphate demand in an intermittently restricted basin[12].

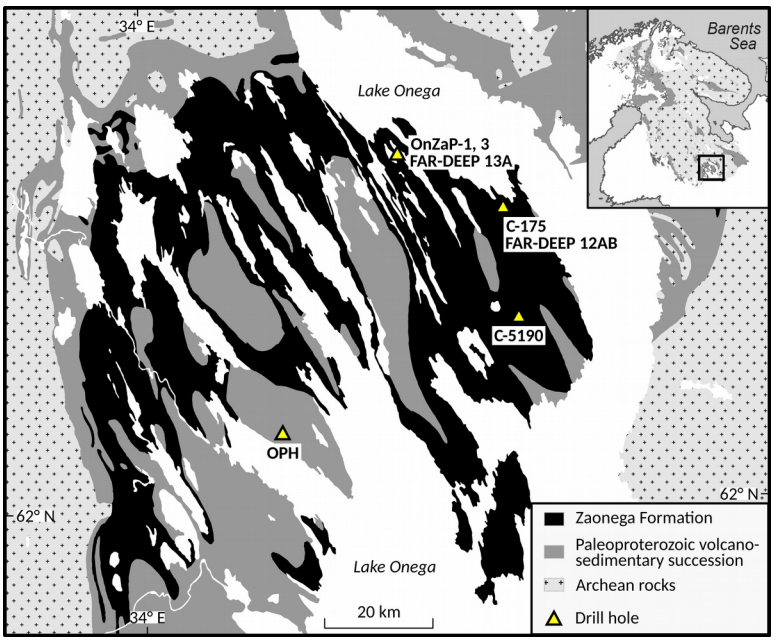

Figure S1: The Zaonega Formation and the positions of the discussed drill cores in the context of the Paleoproterozoic Onega Basin in Karelia, northwestern Russia.

Age constraints of the Zaonega Formation

The upper bound for the age of the ZF canonically relies on the occurrence of ^{13}C-enriched carbonate rocks in the underlying Tulomozero Formation and the lowermost ZF[3,7]. These are viewed as recording the Lomagundi-Jatuli Event (LJE),

which terminated in Fennoscandia at ~2060 Ma[13,14]. The lower constraint is provided by cross-cutting dykes, dated 1919±18 Ma[15], 1956±5 Ma[16], and 1961±5.1 Ma[17], as well as gabbro sills of the overlying Suisari Formation, dated to 1969±18 Ma[18] and 1988±34 Ma[19]. The depositional age constraint on the ZF was recently provided by Martin *et al.*[17], who dated a tuff in the lower part of the ZF to 1982±4.5 Ma. Although this new date has yet to be independently confirmed, we provisionally adopt a ~1980 Ma age for the ZF.

Fluid alteration effects

If RSE concentrations in the ZF are to be used to make global inferences about the paleoredox conditions contemporaneous to deposition, it must be determined if these enrichments are primary (i.e., representative of seawater) or the result of a secondary diagenetic/metamorphic overprinting. Many of the samples with the highest RSE concentrations in the OnZaP section are found in the 77–70 m and 53–44 m intervals (Figure 1). These intervals show evidence of alteration, including features characteristic of soft-sediment deformation, veining, and silicification[12]. Furthermore, hydrocarbon generation and migration is known to have occurred in the ZF[1,5,9,11]. These modifications occurred shortly following deposition, triggered by syn-depositional magmatic activity and the emplacement of gabbro sills into unlithified, wet sediments[5,9].

Nonetheless, there are a number of lines of evidence that these secondary processes had a limited effect on the inventory of RSE. First, the highest Mo enrichments correspond to the highest Mo isotope ratios (1.49±0.14‰; Figure 1) which is inconsistent with Mo being introduced by hydrothermal fluids that are characterized by low $\delta^{98/95}$Mo values of 0.04±1.04‰[20,21]. Second, oil is generally depleted in Mo[22–24] and migrating hydrocarbons in the upper ZF have been shown to be locally sourced[9,11], indicating only a minor effect on larger-scale RSE trends. Third, Mo and U enrichments within the confined interval in the upper ZF extend

over the breadth of the Onega Basin, and are present in both the OnZaP and OPH sections that are separated by 60 km (Figures 1, S1 and S2). This clearly points to a basin-wide enrichment, instead of localized hydrothermal systems. Mo enrichments have also been reported from core C-175 studied by Asael *et al.*[25] and cores FAR-DEEP 13A and 12AB studied by Lepland *et al.*[10], all of which can be correlated to the studied OnZaP and OPH sections[26]. The most parsimonious explanation for the basin-wide enrichments, therefore, is a depositional event initiated by the establishment of transient water column conditions that were conducive to the sequestration of RSE.

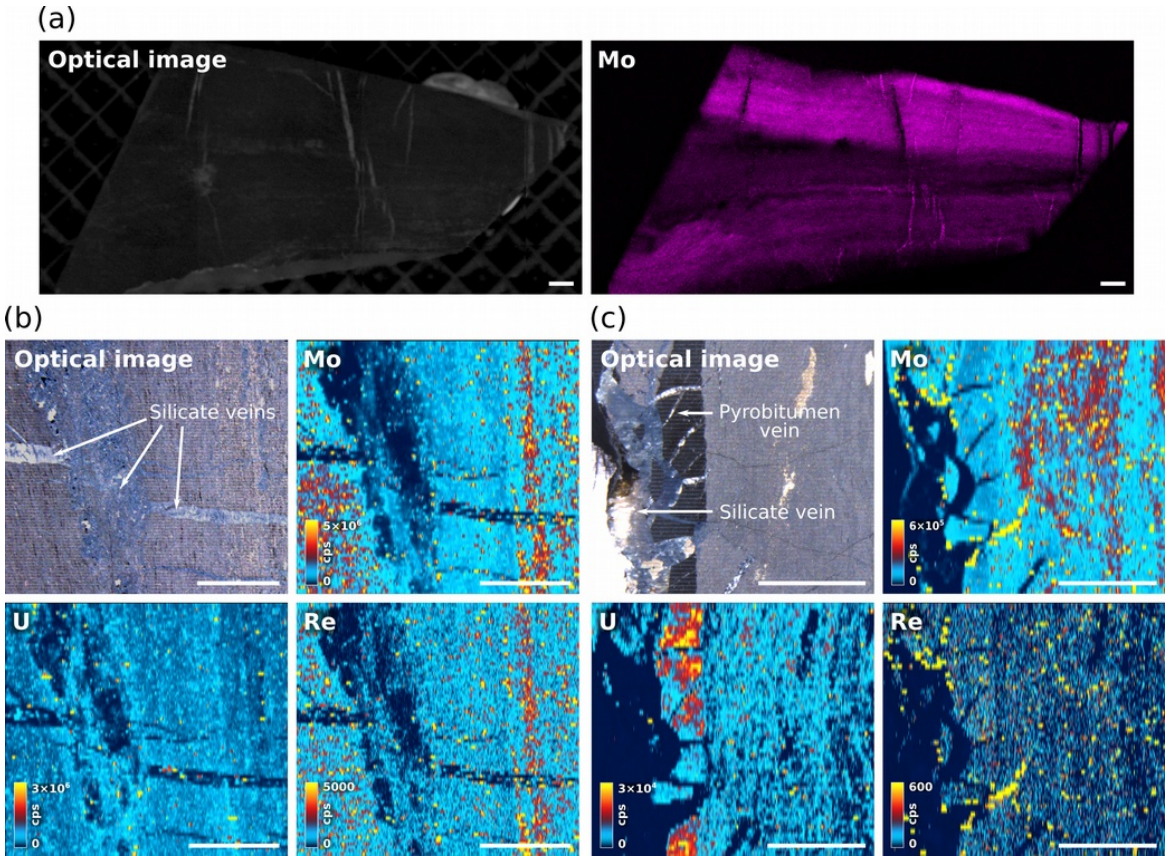

Figure S2: Distribution of RSE in Zaonega Formation mudstones and cross-cutting veins. (a) Optical microscope image and µXRF Mo abundance map of sample 4000943 slab (depth 46.36 m in the OnZaP section). (b) Optical microscope image and corresponding LA-ICP-MS abundance maps of Mo, U, and Re of sample 4000943 slab (depth 46.36 m in OnZaP section); bulk abundance 1009 µg g^{-1} of Mo, 34 µg g^{-1}

of U, and 468 µg g^{-1} of Re. (c) Optical microscope image and corresponding LA-ICP-MS abundance maps of sample 4000988 slab (depth 74.35 m in OnZaP section); bulk abundance 291 µg g^{-1} of Mo, 50 µg g^{-1} of U, and 111 µg g^{-1} of Re. Scale bars represent 2 mm.

In-situ microscale RSE mapping of rock slabs from the OnZaP section was used to further determine the potential role of hydrothermal and pyrobitumen veining on RSE distribution in the upper ZF. Microscale X-ray fluorescence (µXRF) mapping shows that Mo in RSE-replete horizons of the upper ZF is predominantly associated with laminated mudstone comprising the host rock, with individual laminae having variable concentrations (Figure S3). Cross-cutting quartz and phyllosilicate veins permeate the sediments and occasionally act to concentrate Mo at vein margins, but have a negligible effect on bulk Mo concentration. Moreover, mudstones show Mo depletion at contacts to silicate veins, suggesting that any Mo mobilized was locally derived from the host mudstone and subsequently redistributed.

Laser ablation inductively coupled plasma mass spectrometry (LA-ICP-MS) mapping corroborates the observations from µXRF (Figure S2). Mo is predominantly present in laminated sediments and seems to be much less abundant in silicate veins (though some minor concentration is observed on vein edges). Pyrobitumen veins are devoid of Mo, yet seem to concentrate U. Re follows a similar pattern to Mo, but shows a slight preference to pyrobitumen, compared to Mo (Figure S3b). Overall, these data preclude a significant role of veining on RSE distribution in the ZF (with the possible exception of U), even on a per-sample basis. Therefore, we suggest that Mo and U concentrations >100 µg g^{-1}, and Re >100 ng g^{-1}, can likely be regarded as primary environmental signals.

Factors controlling RSE accumulation in sediments

As a consequence of RSE reactivity under different redox conditions[27,28], black shales effectively sequester Mo, U, and Re proportionally to their concentration in the overlying water column, which is in turn tied to the relative global proportion of

marine oxic to anoxic water column conditions[29–31]. This inference has led to several large-scale temporal surveys of RSE in black shales that generally supported a four-stage history of ocean oxygenation (Figure 2)[29,30,32]. Low trace metal abundances in the Archean (generally <10 μg g^{-1} Mo and U, as well as <30 ng g^{-1} Re) point to prevailing anoxia with possible transient O_2. Moderate increases in RSE concentrations in the Paleoproterozoic (up to 100 μg g^{-1} Mo, 60 μg g^{-1} U, and 180 ng g^{-1} Re) are followed by a decline in the mid-Proterozoic, interpreted to reflect the rise and then a decline of ocean–atmosphere O_2 levels[29,33,34]. A conspicuous increase in RSE in black shales starting in the Neoproterozoic (up to thousands of μg g^{-1} Mo, 500 μg g^{-1} U, and 1000 ng g^{-1} Re) is consistent with the rise of O_2 to near-modern levels and the terminal oxygenation of the oceans[35,36].

While compilations such as these rely on averaging of local conditions over many sections, it is important for our study to consider alternative mechanisms that can affect local RSE abundance. For instance, there are several factors that can explain low RSE concentrations without the need to invoke a predominantly anoxic ocean. Firstly, poor connectivity of the basin to the open ocean can lead to local drawdown of RSE—in the isolated Black Sea, euxinic conditions have resulted in highly efficient Mo drawdown leaving only ~0.3 nM of Mo in the bottom water and relatively low Mo concentrations of <40 μg g^{-1} in the topmost sediments[31]. Secondly, local RSE abundance is dependent on the uniformity or heterogeneity of RSE concentrations throughout the oceans, which is ensured in the modern by RSE residence times exceeding the mean ocean mixing time[27,37,38]. Poorly oxygenated oceans, however, must have lowered RSE residence times, which may have resulted in anomalously low sedimentary RSE concentrations where local RSE drawdown exceeded lateral input, even if the local basin wasn't strictly isolated. Third, inefficient Mo scavenging under low HS^- conditions can lead to low sedimentary Mo concentrations even in open-marine conditions[39].

In contrast, it is much more difficult to explain elevated RSE concentrations in black shales in a way that does not rely on the presence of a large global marine RSE

pool. Nevertheless, one important factor to consider is sedimentation rate—a longer residence time of sediments in the zone of RSE diffusion near the sediment-water interface will allow for higher accumulation of RSE[40]. For example, low sedimentation rates have been linked to high TOC accumulation in the U-rich black shales of the Miocene Monterey Formation, USA[41]. While it is possible that low sedimentation rates enhance TOC and RSE accumulation in the ZF, it is unlikely that they were the primary control—the magnitude of RSE enrichment, rivalling Phanerozoic levels (Figure 2), requires an oxygenated, RSE-rich marine pool to draw upon. This is independently confirmed by highly enriched δ^{238}U data that require low rates of global anoxic U drawdown (Figure 2)[40]. Another remote possibility is that, if the Onega Basin was highly restricted, the local RSE pool could have been enriched by the weathering flux from a proximal RSE-rich ore body. However, given that the RSE-enriched horizon, several tens of meters thick, extends throughout the ~200 km diameter basin, it is implausible for the implied volumes of RSE to be supplied by a single point weathering source. Furthermore, the highest $\delta^{98/95}$Mo values occur in the parts of the section that have highest Mo concentrations (Figure 1). Had most of the Mo in that interval been derived from the weathering of a proximal Mo-rich ore body, $\delta^{98/95}$Mo would instead be expected to correspond to values around ~0.3‰ that are characteristic of igneous Mo-bearing sulphide minerals[20]. A more likely explanation for RSE enrichment, then, is that the ZF was a highly efficient RSE sink that had reliable access to a large oceanic RSE inventory (though some modest restriction was required to sequester appreciable amounts of Mo[31,36]).

Redox evolution in the upper ZF

Primary changes in RSE abundance through the upper ZF should reflect changes in redox and hydrographic conditions during deposition. Indeed, RSE trends through the OnZaP and OPH sections agree well with independent studies on the redox

evolution of the upper ZF[2,8–12]. Based on petrological and sedimentological features, such as intermittent turbidites, peperite contacts marking the emplacement of mafic intrusions in wet, unconsolidated sediments, pyrobitumen veining, and phosphorite layers, the ZF is thought to mostly represent deep water deposition in a magmatically active basin that experienced hydrocarbon generation/seepage[2,8] and redox fluctuations. Paiste *et al.*[12] has shown that these conditions extend to the 102–44 m interval in the OnZaP section and that the interval was also host to an active methane and S-cycling microbial community[9–12].

Our RSE data support this interpretation, with Mo, U, and Re all following similar trends. Mo concentrations, for example, remain below 95 µg g^{-1} in the lower part of the OnZaP section until ~80 m depth, above which they increase gradually up to ~400 µg g^{-1} at 53 m, consistent with the onset of anoxia and more efficient RSE drawdown (Figure 1). While the presence of early-diagenetic pyrite in the form of 30–100 µm-sized ellipsoidal clusters suggests that HS^- was restricted primarily to shallow pore waters throughout most of the OnZaP section[12], highly enriched and variable RSE content in the 53–44 m interval (Mo concentrations vary between ~20–1000 µg g^{-1} and reach their highest value at 46 m depth) shows that redox conditions became significantly more variable. This is supported by the occurrence of phosphorite layers in the same interval (Figure S6)—correlative samples form a nearby outcrop have been shown to bare putative indication of phosphogenic S-cycling microbes inhabiting a fluctuating sulphidic–(sub)oxic redoxcline close to the water–sediment interface[10]. Variable redox conditions may have been the result of intermittent basin restriction, similar to modern anoxic basins[42], where periodic inputs of oxic water replenish RSE that are then sequestered in sediments when euxinia develops during stagnant periods. Above 44 m depth, TOC and pyrite abundance gradually decreases, until petrographic markers of potentially shallower and more restricted hydrographic conditions become present at 33 m[12]. Furthermore, increasing $\delta^{13}C_{org}$ and $\delta^{34}S$ values have been used to suggest a change to variable (sub)oxic conditions[12]. This shift is also borne out by decreasing Mo and

U abundances that approach crustal levels above 33 m (Mo concentrations fall to below 10 μg g^{-1}; Figure 1), whereas Re, which also accumulates in suboxic conditions, remains partially enriched above 2 ng g^{-1} (Ref. 43). Collectively, redox conditions in the OnZaP section were most favourable for the drawdown of RSE during the deposition of organic-rich mudstones intercalated with dolostone beds at depths between 76–44 m.

Molybdenum isotopes

The Mo isotope system provides additional constraints on marine Mo cycling and ocean redox conditions[44]. The most significant input of Mo to the oceans is riverine transport of dissolved MoO_4^{2-}, which has a modern average $\delta^{98/95}$Mo of ~0.2‰[44,45]. Amongst the sinks, Mo adsorption to Mn(IV)-oxides in oxic environments is the most consequential, as it imparts the largest isotope fractionation at about −3.3‰[44,46]. However, in strongly euxinic environments, Mo removal into sediments is often near-quantitative with only minor fractionation[44,46–48]. Intermediate redox conditions lead to variable Mo fractionation from seawater to sediment; an average of about −0.7‰ is commonly assumed[49–53]. Due to widespread oxic conditions in modern oceans and the large fractionation imparted by adsorption onto Mn(IV)-oxides, the residual marine pool has been enriched to 2.36‰ $\delta^{98/95}$Mo[44,46,54]. Accordingly, less oxidized marine conditions in the Proterozoic would have been characterized by lower seawater $\delta^{98/95}$Mo values[47]. It also follows that strongly sulphidic sediments, where Mo removal is quantitative, can faithfully record this signal, allowing the use of black shale $\delta^{98/95}$Mo as a paleoredox proxy[21,46–48].

Despite the ZF being predominantly a black shale succession, interpreting the Mo isotope record in the OnZaP section is difficult for several reasons. Under euxinic conditions with HS^- <11 μM, fractionation between intermediate thiomolybdate species can result in significant offsets between seawater and sediment $\delta^{98/95}$Mo[48,55–

[57], and verifying euxinia in the upper ZF section has proven difficult. Fe speciation, the most-accepted method for tracking euxinic conditions[58,59], can be affected by Fe mobilization and (re-)precipitation[60]. Fe speciation is biased in the upper ZF due to the presence of Fe-rich carbonates and secondary pyrrhotite[12,61]. Early diagenetic pyrite, evident as 30–100 µm-sized ellipsoidal clusters, have been taken as evidence for the restriction of HS^- to pore waters[12], and so has phosphorite accumulation in the same interval[10] (Figure 1). Modern phosphorites do not accumulate in euxinic basins, but rather in suboxic ones with euxinia confined to the immediate subsurface, as is preferred by polyphosphate-cycling microorganisms[62]. In contrast, enriched $\delta^{238}U$ values suggest euxinia, as such values require U reduction in the water column; the latter of which likely scales with S reduction rates[40,63].

The second prerequisite for quantitative Mo drawdown is the establishment of a restricted basin[31,64–66]. The $\delta^{98/95}Mo$ of modern seawater (2.36‰) is only captured in sediments of the heavily restricted Black Sea[31,48], while sediments in the less restricted, but HS^--replete Cariaco Basin are fractionated by about −0.7‰ from seawater values[31,47]. Partial restriction of the Onega basin has been suggested to explain S-isotope systematics in the ZF[12], and some restriction is required to capture non-trivial amounts of Mo in sediments[31]. However, as discussed above, tens of meters of sediment with a Mo concentration over several hundred µg g^{-1} could not have accumulated in a Black Sea-like setting without relatively frequent deep water replenishment. Furthermore, Kurzweil *et al.*[64] suggested that a negative correlation between $\delta^{98/95}Mo$ and Mo concentrations would be indicative of a Mo drawdown regime favourable for quantitative capture, but the reverse is observed in the OnZaP section—Mo isotope ratios show a positive tendency with increasing Mo concentrations (Figure S3), suggesting that Mo was not quantitatively sequestered in the ZF. Accordingly, the sedimentary $\delta^{98/95}Mo$ recorded in the upper ZF should be somewhat depleted relative to seawater[65].

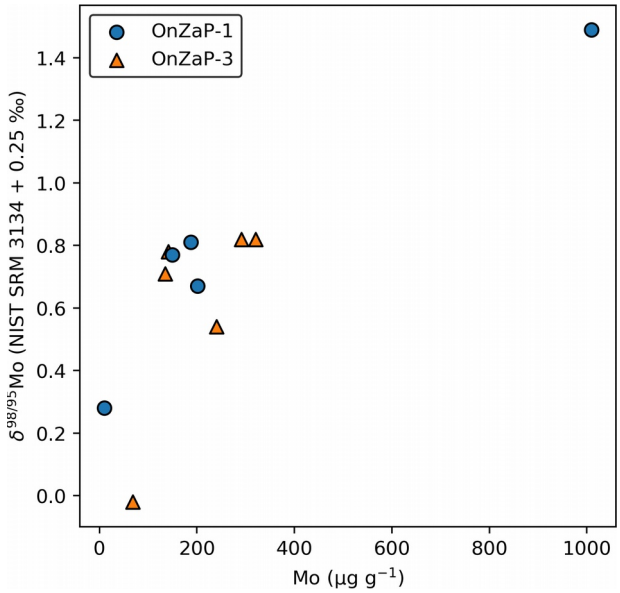

Figure S3: Crossplot of Mo concentration and $\delta^{98/95}$Mo in the OnZaP section.

Given that almost all known Mo fractionation processes lead to the depletion of ^{98}Mo in sediments[21], the $\delta^{98/95}$Mo data presented here can be considered a minimum estimate for seawater at ~2.0 Ga. In the OnZaP section, average $\delta^{98/95}$Mo is relatively low at 0.67±0.81‰, but reaches a maximum of 1.49±0.14‰ at 46.36 m (Figure 1). While this isolated maximum value could be anomalous, similar values have been reported from the ZF interval ~50 m below the OnZaP section in the core FAR-DEEP 13A (as correlated via a P-rich dolostone marker horizon, see Materials and Ref. 26), drilled 200 m from the OnZaP drilling sites[61]. Though samples from euxinic intervals in Asael *et al.*[61] had a similarly low average $\delta^{98/95}$Mo of 0.73±0.21‰, three measurements exceeded 1‰, with a maximum value of 1.29±0.11‰. Likewise, Asael *et al.*[25] examined the C-175 and C-5190 cores (drilled ~20 and ~40 km from the OnZaP site, respectively, and possibly representing a stratigraphic section of the upper ZF beginning >300 m below the OnZaP section and extending to its lower half[26]), where samples from euxinic intervals had an average $\delta^{98/95}$Mo of 0.70±0.21‰, with eight measurements surpassing 1‰, and some reaching as high as 1.83±0.11‰. These authors considered averages of samples from euxinic

intervals representative of seawater $\delta^{98/95}$Mo with the highest values attributed to distillation effects in a temporarily restricted basin[61].

Alternatively, we propose that the requisite conditions for quantitative capture of seawater $\delta^{98/95}$Mo were effectively absent during deposition of the upper ZF, either due to relatively open-marine conditions, insufficient water column HS^-, or Mn(IV)-oxide cycling. Given this view, the small number samples in the ZF that record values ≥1.4‰ likely represent periods of more quantitative capture of seawater values that may be attributed to increased basinal restriction or transient increases in water column HS^-. A minimum seawater $\delta^{98/95}$Mo value of ~1.4‰ is comparable to other Proterozoic successions, including those deposited during the LJE[25,67], but is modest compared to Phanerozoic seawater. Thus, the Mo isotope record in the ZF is compatible with an oxygenated ocean but cannot itself preclude anoxic conditions.

Uranium isotopes

Redox processes in marine environments have been found to induce significant U isotope fractionation[68], allowing the U isotope system to become widely utilized in paleoredox studies. Oceanic δ^{238}U in the modern world is –0.39±0.01‰[69] and varies little in the open ocean, as U is present in oxic seawater as uranyl $[U(VI)O_2]^{2+}$ that forms highly stable carbonate complexes; as such, the residence time of U in seawater is in the order of ~400 kyrs[70], far exceeding the ~1 kyr ocean mixing time[71]. Seawater δ^{238}U reflect the balance between the riverine U source, and between different sedimentary U sinks. Rivers, being the major U input into oceans[72], carry a mean δ^{238}U value of ~−0.34‰[73], within error of estimates of the −0.29±0.03‰ continental crust[69]. Amongst major sinks, anoxic sediments and euxinic sediments prefer ^{238}U, leaving residual seawater depleted in comparison to riverine inputs[74]. Mn- and Fe-oxides bury isotopically light U, but this is a relatively minor sink[74]. Incorporation into carbonates formed in the water column is generally

thought to impart only minor fractionation on U isotopes[75]. Hydrothermal processes operating at mid-ocean ridges cycle seawater U through hot, highly reducing, deep mafic rocks, where U is reduced and incorporated into altered oceanic crust. This can be quantitative or impart a positive δ^{238}U fractionation[76,77]. Sediments underlying fully anoxic waters have the great potential to shape seawater δ^{238}U values. These constitute the most effective U sinks per unit of area[72] and effect the highest fractionation from seawater δ^{238}U. Modern anoxic basin sediments contain values between −0.2‰ and 0.4‰; even larger fractionations are possible when reduction happens in the water column instead of the sediment pile[74]. The marine U pool is highly sensitive to the extent of strongly anoxic basins and at times in Earth history where the anoxic sink was increased in prevalence—e.g., at times of lower oxygenation in the Precambrian—seawater δ^{238}U is expected to have been lower.

Therefore, there has been extensive research targeting the U isotope composition of ancient sediments that can record seawater δ^{238}U as a proxy for the oxygenation of the ocean–atmosphere system (see Ref. 74 for overview). The first sedimentary δ^{238}U enrichments are reported from the Meso- and Neoarchean, suggesting oxic weathering, local U burial in anoxic sediments, and at least locally depleted δ^{238}U compared to modern seawater values[78,79]. δ^{238}U values increase in the Paleoproterozoic[79], whereas the mid-Proterozoic record is, as of yet, sparse: carbonates from the time period display δ^{238}U values similar to modern seawater, implying limited marine euxinia[80], while shale δ^{238}U allow for more anoxic conditions[81]. A near-modern seawater U balance is thought to have been established by the Ediacaran[82], with some fluctuations associated with Phanerozoic anoxic events (e.g., Ref. 83).

Aside from carbonates, many studies utilize anoxic shales as δ^{238}U archives. Uranium fractionation in anoxic sediments is imparted during the reduction of uranyl to U(IV) that, given the slow kinetics, is thought to occur mainly in sediment pore waters, catalyzed by microbial enzymes[28]. Experimental and modelling studies suggest that the equilibrium fractionation factor in U reduction is ~1.2‰ (e.g., Refs.

74, 84, 85), yet given diffusion limitations into the sediments, the effective fractionation is normally half of that[40]. Interpretation of shale δ^{238}U is complicated by several factors. (1) The extent of fractionation from seawater to anoxic shales is highly dependent on the specific redox state of the depositional environment, i.e., the depth of oxygen penetration into sediments or the redox state of the bottom waters[40]. (2) Basinal restriction, like in the modern Black Sea[86], can lead to significant bottom water U drawdown and modulation of local seawater δ^{238}U due to back-diffusion of depleted sediment pore water. The result is significant difference between the effective and intrinsic fractionation[74]. (3) If sedimentation rates are high, detrital or carbonate contamination may play a large part in the sediment U budget and isotope composition; methods have been developed to correct for such contamination (e.g., Refs. 61, 73). (4) In the Precambrian, the prevalence of anoxic basins might have resulted in effective U drawdown and short seawater U residence times[29]; due to the δ^{238}U variability of local riverine input (−0.70 to 0.06‰ in the modern[73]), seawater δ^{238}U might then have become heterogeneous, and could have ceased to reflect global, as opposed to local, U cycling[74]. In summation, there are several possible non-unique ocean redox states for most shale δ^{238}U values.

That the ZF contains anomalously high U concentrations (up to 238 μg g^{-1}, rivalling even modern sediments in anoxic settings), however, imposes significant constraints on these uncertainties. These concentrations require that the Onega Basin retained reliable access to an extensive marine U pool during ZF deposition, which precludes the possibility of the local marine δ^{238}U being affected either by ocean U heterogeneity or local water column U depletion. Significant detrital or carbonate contamination is, likewise, negated by the high total U content. The average U content of our δ^{238}U samples is 55±41 μg g^{-1}, whereas the upper crust, a proxy for detrital material, only contains 2.7 μg g^{-1} of U on average[87] and primary carbonates ~1 μg g^{-1} (Ref. 75)—hence, only a minor fraction of U could be derived from contamination in these samples.

The U isotope composition in the ZF is, therefore, a product of local water column and sediment redox conditions and the balance of marine U sinks, i.e., global marine redox conditions. Our average δ^{238}U is 0.48±0.28‰, whereas the highest values, up to 0.79‰, are anomalous in the shale δ^{238}U record (Figure 2). The typical fractionation between anoxic water columns and the underlying sediments is 0.6–0.8‰[40], and subtracting that from our data, we would arrive at an average estimated seawater δ^{238}U between –0.32 to –0.12‰. These values are somewhat higher, but comparable, to the modern –0.39‰ seawater value and imply a near-modern or lesser significance of anoxic basins as a marine U sink. However, it is not possible to explain the highest δ^{238}U values of nearly 0.8‰ merely by modulating the extent of ocean anoxia—one would arrive at seawater δ^{238}U values exceeding the average crustal source of −0.29‰[69], which is considered highly unlikely in the current understanding of marine U systematics[74]. Instead, the effective fractionation between anoxic seawater and the underlying sediments must have exceeded the typical values[40], likely due to a shift in the locus of U reduction into the water column, as is observed in Unit II of the Black Sea[40]. Water column U reduction requires high organic matter loading and high water column sulphate reduction rates. This conclusion is not unexcepted—the ZF is known for extraordinary C_{org} abundance that must, in part, be attributed to a highly productive local ecosystem (e.g., Refs. 9, 10, and 12). Further, the ZF δ^{238}U data require seawater δ^{238}U values not substantially lower than the modern value, which in turn requires a prevalence of euxinic conditions on the seafloor similar to, or lower than, the modern world.

The ZF δ^{238}U record has previously been studied by Asael et al.[61] from a section of the FAR-DEEP 13A core (drilled close to the OnZaP coring sites, but ~50 m lower in stratigraphy[26]; Figure 1). These data, despite being significantly more depleted, are consistent with our findings—even though their measured δ^{238}U averaged only 0.07±0.18‰, this was likely due to the significantly lower U concentrations in their samples, on average 5±3 μg g^{-1}. In such a case, the detrital component could exert a large effect on sample δ^{238}U composition. After being corrected for detritus, the

average shifted to 0.35±0.22‰, placing these values well within the uncertainty expected for different burial U isotope fractionations. Further, given the low enrichments in the FAR-DEEP 13A core, U(VI) reduction almost certainty occurred within the sediment pile leading to a muted fractionation.

RSE normalized to organic carbon content

Total organic carbon in the OnZaP section and the studied OPH section is amongst the highest of all sections included in RSE compilations[29,30,32], and as such, RSE concentrations in the upper ZF are slightly muted when normalized to TOC. Even so, the normalized RSE abundances still rank among the highest before the Neoproterozoic, supporting our interpretations of a large marine RSE inventory (Figure S5).

A linear relationship between sediment Mo and TOC content has been observed in many modern and ancient euxinic basins, a result of the importance of organic phases in scavenging Mo from anoxic waters[31,57,89,90]. A seminal study by Algeo & Lyons[31] found that in restricted anoxic basins, Mo/TOC ratios in organic-rich sediments scale with deep water Mo concentration, allowing for its use in constraining local hydrographic and redox conditions. Deep water Mo concentration has a first-order dependency on the size of the marine Mo pool, but is modulated by the degree of deep water restriction because if water exchange is limited, anoxic Mo scavenging rates can exceed the replenishment rates, leading to depletion of dissolved Mo[31]. The highest sediment Mo/TOC was found in weakly restricted basins with intermittently or weakly euxinic bottom waters, where deep water flushing events are sufficiently common that Mo is not drawn down significantly, but where HS^- could still accumulate enough to convert MoO_4^{2-} to particle-reactive $MoO_xS_{4-x}^{2-}$ phases[31,39]. This effect is amplified by the efficient operation of the Mn(IV)-oxide shuttle in mildly or intermittently euxinic conditions[31,37,91–93]. Since the oxidation state of the oceans is poorly constrained in the Precambrian, Mo/TOC serves mainly

as a proxy of deep water Mo concentrations, which can be related to the size of the global marine Mo pool only if local basinal restriction can be constrained via independent means.

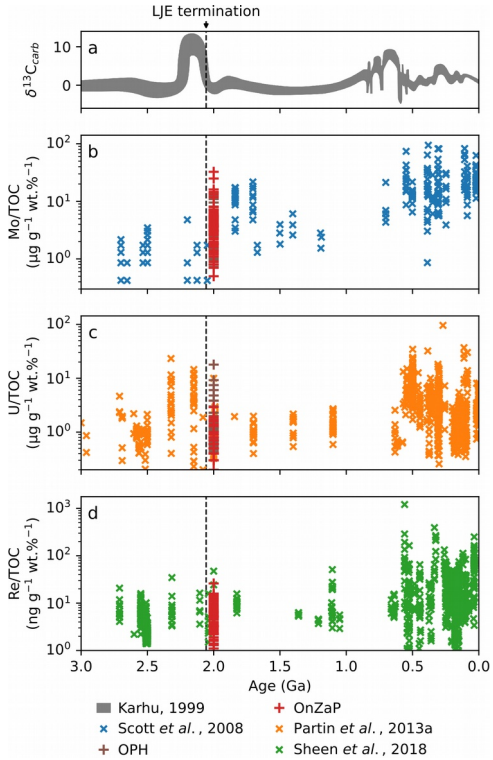

Figure S4: Secular trends in $\delta^{13}C_{carb}$, as well as Mo/TOC, U/TOC and Re/TOC ratios of anoxic shales. Data from Karhu[88], Scott *et al.*[32], Partin *et al.*[29] and Sheen *et al.*[30], respectively, along with measurements from this study.

The average slope of Mo/TOC covariation in non-carbonate/organic-rich samples of the ZF is 5.11 µg g^{-1} wt.%$^{-1}$, comparable to the modern Black Sea, in which deep water Mo is 0.2–0.3 nM, ~20–30 times less than the open ocean on a salinity-normalized basis (Figure S6)[31]. The exceptions are the 78–70 m and 53–44 m intervals of the OnZaP section, and the 1125–1100 m interval in the OPH core, where Mo/TOC reaches maximum values of 32.6 µg g^{-1} wt.%$^{-1}$ and 13.85 µg g^{-1} wt.%$^{-1}$, respectively. These relatively enriched intervals could represent periods when the ZF entered the type of hydrographic conditions most susceptible to Mo

scavenging i.e., mild and intermittent deep water restriction and a fluctuating and weak euxinia. This is supported by the co-occurrence of the highly variable Mo concentrations in that same interval (Figure 1, S2).

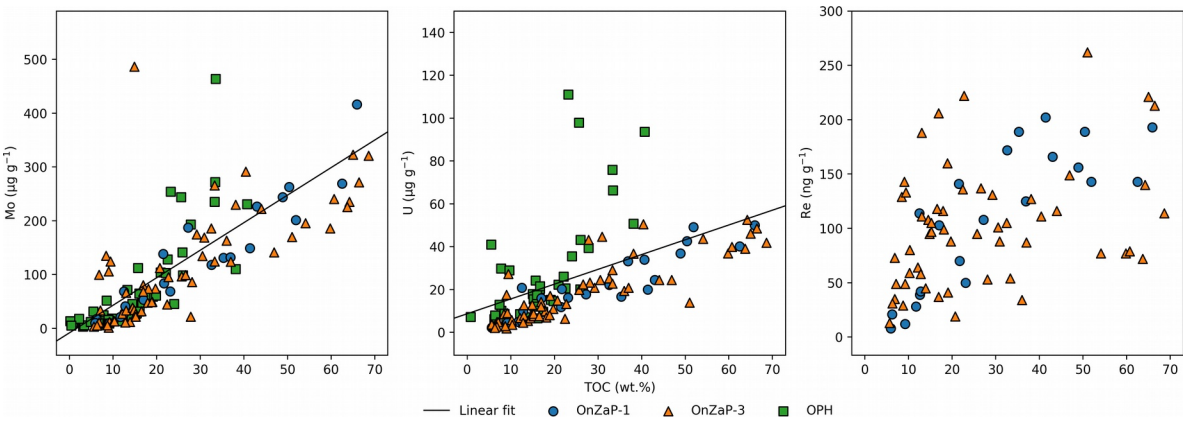

Figure S5: Covariation of total organic carbon (TOC) and RSE concentrations in the OnZaP section and OPH core.

Despite these intervals of high values, the dominant Mo/TOC trend of 5.11 µg g^{-1} $wt.\%^{-1}$ is modest, in a puzzling contrast to the extremely high Mo concentrations. There are several potential explanations for this discrepancy. First, it is possible that upper ZF sediments, containing >60 wt.% TOC, were sufficiently efficient at scavenging trace metals to deplete the local deep water of dissolved Mo even under conditions of only modest restriction. Further work on the applicability of the Mo/TOC proxy in situations of high organic matter accumulation is needed to test this; Algeo & Lyons[31] only calibrated their proxy up to 20 wt.% TOC. Second, if the Onega basin had a relatively unrestricted connection to the ocean, rapid water mixing would have made water column HS^- accumulation rare, precluding the presence of particle reactive Mo phases. The unrestricted modern Namibian shelf, for example, has a sediment Mo/TOC ratio of only ~6±3 µg g^{-1} $wt.\%^{-1}$, despite abundant deep water Mo[31]. This interpretation is supported by Paiste *et al.*[12], who, based on pyrite petrography, argued that HS^- in the ZF was confined mostly to pore waters. Third, the applicability of the Mo/TOC proxy to Precambrian sediments is

questionable in itself. Algeo & Lyons[31] considered that a wholesale drawdown of the trace metal inventory during global anoxia might fundamentally change the Mo–TOC relationship, so that their calibration might not hold. Furthermore, the average composition of marine organic matter and how it was processed in the sediment pile might have been somewhat different in the Paleoproterozoic, affecting its reactivity to trace metals.

Enrichment factors

Enrichment factors (EF) are way of presenting RSE content that corrects for the effects of detrital input and facilitates comparison between different elements[93]. The RSE concentrations are corrected for the Al concentration of the sample and the average content of the upper continental crust[94] using the formula $X_{EF} = (X/Al)_{sample}/(X/Al)_{crust}$. In the studied section of the ZF, EFs confirm the high authigenic enrichment of RSE and tightly correspond to TOC and RSE concentrations. Whereas a substantial authigenic enrichment starts at X_{EF} >10[93], Mo_{EF} in the ZF reaches a maximum of 2019, U_{EF} up to 1425, and Re_{EF} up to 6770.

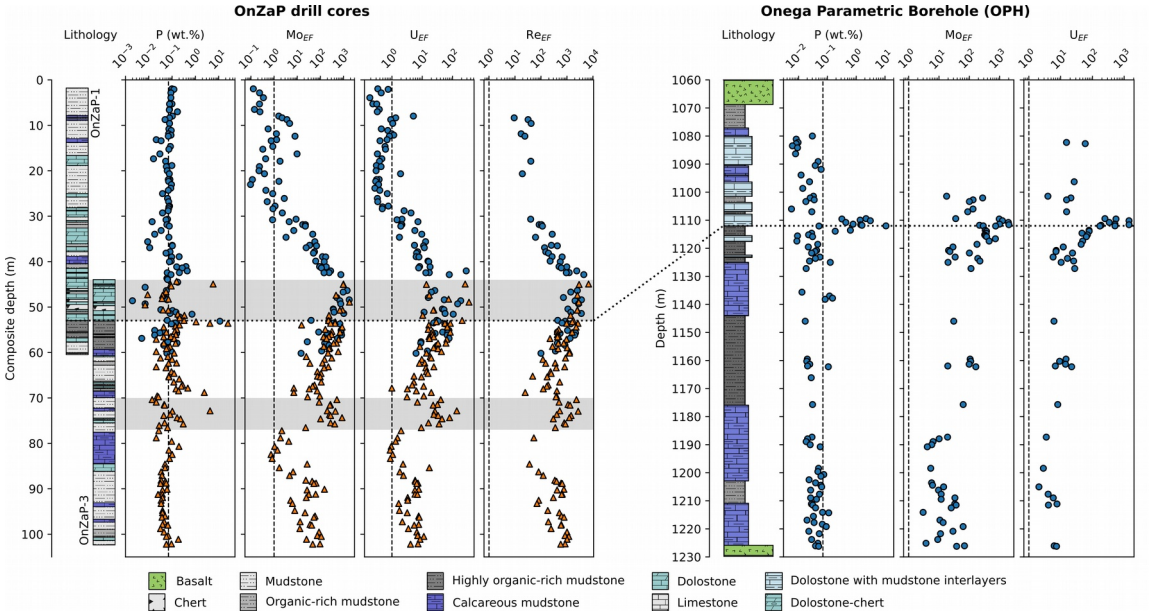

Figure S6: Phosphorous concentrations and redox-sensitive metal enrichment

factors. Phosphorous content illustrates the P-rich mudstone-dolostone contact that is used for intra-basinal correlation. For reference to plot elements see caption of Figure 1 in the manuscript.

Late Paleoproterozoic redox landscape

Redox sensitive element replete conditions during the deposition of the ZF have important implications for global events in related to the redox landscape of the later Paleoproterozoic. For instance, the expansive marine RSE inventory provides strong evidence for the diachronous nature of the Shunga-Francevillian Event, as was first suggested by Martin *et al.*[17]. Although ~2100–1800 Ma black shales are common[95], they cannot all have been synchronous with the ZF, as RSE enrichment in the ZF demonstrates that anoxic conditions cannot have been dominant on the continental shelves. Instead, ferruginous and euxinic conditions must have been relatively rare during deposition of the ZF in order to maintain the marine pools of these RSE. This is critical because it implies the continental shelves were largely overlain by oxygenated seawater.

This observation also has the potential for explaining puzzling gaps in the iron formation (IF) record. Superior-type IF were formed as ferruginous waters upwelled onto shelves where biogeochemical processes oxidized dissolved Fe(II) into Fe(III)-oxyhydroxides[96]. While IF are characteristic of the Precambrian, there are recognizable gaps in their abundance, one of the most prominent having occurred between ~2400–1880 Ma[97]. Holland[98] originally argued that this gap in IF deposition was due to increased oxygenation of marginal marine environments, while Canfield[99] suggested that Fe(II) was instead drawn down by HS^- as a consequence of widespread euxinia fuelled by increased aerobic sulphide weathering. Returning to Holland's idea, our data suggest that widespread oxygenation, not HS^- abundance, shifted the locus of Fe(II) oxidation from continental shelves to the deep oceans where sediments are unlikely to be preserved during the tectonic recycling of the oceanic crust.

However, there remains a substantial preponderance of evidence for a return to lower O_2 levels in the later Paleoproterozoic, including a decrease in marine sulphate levels[100,101], a global proliferation of anoxic basins[95], the a return of RSE concentrations to near-Archean-like levels[29,102], a sharp decrease in Mo isotope ratios in black shales[25], a shift towards reduced Fe burial[103,104], and geochemical indications for relatively low mid-Proterozoic ocean-atmosphere O_2 levels moving into the mid-Proterozoic[105–108]. Whereas our data shows that this major shift in Paleoproterozoic redox landscape did not occur at the end of the LJE (or, possibly, that the redox landscape became highly variable, not uniformly anoxic, after the end of the LJE), then the brief resurgence of IF deposition after 1880 Ma (e.g., Gunflint IF) can possibly signify a general transition from oxygenated to ferruginous conditions on continental shelves, consistent with recent fine-grained rare earth element analyses that found no significant Ce anomaly in the ~1870 Ma Pethei Group[108]. In this regard, our results diverge from earlier views of middle Paleoproterozoic redox evolution which suggested that the Gunflint IF represents the end stage of a 2100–1840 Ma post-LJE deoxygenation event[104].

Supplementary methods

Mo isotopes

Mo isotopes were measured from digested OnZaP MSP0010 samples and all preparation was done in a class 1000 clean laboratory using Mo-free chemicals and equipment. Samples were doped with a ^{97}Mo–^{100}Mo double spike in a constant ratio of spike/sample in order to track any isotopic fractionation during sample purification and to correct for instrumental mass bias[109]. Mo was purified via two-stage column chromatography adapting from the protocol of Asael *et al.*[61], using Biorad AG 1-X8 anion exchange resin and Biorad AG 50W-X8 cation exchange resin. The purified Mo solution was measured for isotopic composition in the Pôle Spectrométrie Océan, IFREMER, Brest, France, using a Thermo Scientific Neptune

multicollector ICP-MS. $\delta^{98/95}$Mo was obtained through the double spike deconvolution method of Siebert *et al.*[109]. Each sample was bracketed with and corrected to measurements of the in-house standard Mo-SPEX that demonstrated a 2SD reproducibility of 0.13‰. Data were acquired relative to Mo-SPEX and expressed relative to NIST SRM 3134 = 0.25‰[110], as per the following equations:

$$\delta^{98/95}\mathrm{Mo}_{\text{Mo-SPEX}} = \delta^{98/95}\mathrm{Mo}_{\text{RochMo2}} - 0.05\pm0.06‰^{61};$$

$$\delta^{98/95}\mathrm{Mo}_{\text{RochMo2}} = \delta^{98/95}\mathrm{Mo}_{\text{SRM3134}} - 0.34\pm0.05‰^{111}.$$

U isotopes

Uranium isotopes of samples from the OPH drill core were measured at the Yale Metal Geochemistry Center, Yale University, USA. Sample digestion, U separation, and isotope measurements were performed in a Pico-trace clean laboratory. The samples were digested in a mixture of 3 ml concentrated HNO_3 and 1 ml HF at 100°C for 24 hours, evaporated to dryness, then digested in aqua regia at 95°C for another 24 hours, evaporated to dryness, and taken up in 5 ml 3M HNO_3 at 70°C. Uranium separation and isotope measurement followed the method outlined in Ref. 79. To monitor instrumental mass bias and potential fractionation during laboratory treatment, the samples were doped with proper amounts of IRMM-3636 233/236 U double spike to yield a $^{238}U/^{236}U$ ratio of ~30 (following Ref. 68). Uranium was separated from matrix elements chromatographically, in columns of UTEVA ion exchange resin (based on Ref. 68; with two stages of column chemistry). Isotope values were measured on a Thermo Neptune Plus MC-ICP-MS, with every set of three samples bracketed by concentration matched CRM 112a standard (New Brunswick Laboratory, USA Dept. of Energy) in order to check for instrumental drift. Accuracy and precision were further monitored with routine measurements of concentration matched standards: CRM129a (New Brunswick Laboratory, USA Dept. of Energy) was −1.71±0.13‰ (2SD, n=27), and in-house Ricca ICP solution was −0.22±0.11‰ (2SD, n=25). These standard measurements agree with the results of

previous studies[112–114]. Instrumental error was found to be less than 0.15‰ in all samples. U isotope ratios are reported in relation to the CRM-112a standard, defined as $\delta^{238}U = 0‰$.

In-situ RSE measurements

µXRF elemental maps were acquired from polished slabs at IUEM, Brest, France using a Bruker Tornado M4 µXRF system equipped with a Si drift detector and a Rh source operating at 50kV and 600 µA. A spot size of 20 µm was employed with a dwell time of 6 ms per pixel, and mapping was performed under vacuum. Image processing included spectral deconvolution and 3-pixel averaging.

LA-ICP-MS measurements were taken from polished slabs in the University of Tartu, Estonia on an Agilent 8800 ICP-MS in single quad mode coupled to a Cetac LSX-213 G2+ laser ablation unit with a HelEx II fast-washout two-volume large-format cell using 800 ml min^{-1} He as carrier gas. Relative element abundance maps of sample 4000943 were interpolated from parallel scans moving left to right at 65 µm s^{-1} with a 65 µm square spot at 10 Hz and laser power of 3.3 J cm^{-2}. Isotopes of ^{13}C, ^{27}Al, ^{28}Si, ^{34}S, ^{47}Ti, ^{51}V, ^{52}Cr, ^{57}Fe, ^{59}Co, ^{60}Ni, ^{63}Cu, ^{66}Zn, ^{75}As, ^{78}Se, ^{95}Mo, and ^{238}U were collected with a dwell time of 8 ms and ^{185}Re with a dwell time of 13 ms, corresponding to a total duty cycle of 0.2 s. Sample 4000988 was, instead, scanned at 33 µm s^{-1} with a 65 µm square spot at 5 Hz and a laser power of 1.65 J cm^{-2}. Isotopes of ^{27}Al, ^{28}Si, ^{34}S, ^{47}Ti, ^{51}V, ^{52}Cr, ^{57}Fe, ^{95}Mo, and ^{238}U were collected with a dwell time of 16 ms and ^{185}Re with a dwell time of 20 ms, corresponding to a total duty cycle of 0.2 s. Maps are presented in counts per second.

References for supplementary information

1. Melezhik, V. A., Fallick, A. E., Filippov, M. M. & Larsen, O. Karelian shungite—an indication of 2.0-Ga-old metamorphosed oil-shale and generation of petroleum: geology, lithology and geochemistry. *Earth-Sci. Rev.* **47**, 1–40 (1999).

2. Melezhik, V. A., Medvedev, P. V. & Svetov, S. A. The Onega Basin. in *Reading the Archive of Earth's Oxygenation* (eds. Melezhik, V. A. et al.) vols 1: The Palaeoproterozoic of Fennoscandia As Context for the Fennoscandian Arctic Russia-Drilling Early Earth Project 387–490 (Springer, Berlin Heidelberg, 2013).
3. Melezhik, V. A., Fallick, A. E., Medvedev, P. V. & Makarikhin, V. V. Extreme $^{13}C_{carb}$ enrichment in ca. 2.0 Ga magnesite–stromatolite–dolomite–`red beds' association in a global context: a case for the world-wide signal enhanced by a local environment. *Earth-Sci. Rev.* **48**, 71–120 (1999).
4. Blättler, C. L. *et al.* Two-billion-year-old evaporites capture Earth's great oxidation. *Science* **360**, 320–323 (2018).
5. Črne, A. E. *et al.* Zaonega Formation: FAR-DEEP Holes 12A and 12B, and neighbouring quarries. in *Reading the Archive of Earth's Oxygenation* (eds. Melezhik, V. A. et al.) vols 2: The Core Archive of the Fennoscandian Arctic Russia-Drilling Early Earth Project 946–1007 (Springer, Berlin Heidelberg, 2013).
6. Črne, A. E. *et al.* Petrography and geochemistry of carbonate rocks of the Paleoproterozoic Zaonega Formation, Russia: Documentation of ^{13}C-depleted non-primary calcite. *Precambrian Res.* **240**, 79–93 (2014).
7. Melezhik, V. A., Fallick, A. E., Brasier, A. T. & Lepland, A. Carbonate deposition in the Palaeoproterozoic Onega basin from Fennoscandia: a spotlight on the transition from the Lomagundi-Jatuli to Shunga events. *Earth-Sci. Rev.* **147**, 65–98 (2015).
8. Melezhik, V. A., Filippov, M. M. & Romashkin, A. E. A giant Palaeoproterozoic deposit of shungite in NW Russia: genesis and practical applications. *Ore Geol. Rev.* **24**, 135–154 (2004).

9. Qu, Y., Črne, A. E., Lepland, A. & van Zuilen, M. A. Methanotrophy in a Paleoproterozoic oil field ecosystem, Zaonega Formation, Karelia, Russia. *Geobiology* **10**, 467–78 (2012).
10. Lepland, A. *et al.* Potential influence of sulphur bacteria on Palaeoproterozoic phosphogenesis. *Nat. Geosci.* **7**, 20–24 (2014).
11. Qu, Y. *et al.* Sample-scale carbon isotopic biosignatures of diverse biomass in the Paleoproterozoic Zaonega Formation, Russia. *Precambrian Res.* **315**, 222–231 (2018).
12. Paiste, K. *et al.* Multiple sulphur isotope records tracking basinal and global processes in the 1.98 Ga Zaonega Formation, NW Russia. *Chem. Geol.* **499**, 151–164 (2018).
13. Karhu, J. A. & Holland, H. D. Carbon isotopes and the rise of atmospheric oxygen. *Geology* **24**, 867–870 (1996).
14. Martin, A. P., Condon, D. J., Prave, A. R. & Lepland, A. A review of temporal constraints for the Palaeoproterozoic large, positive carbonate carbon isotope excursion (the Lomagundi–Jatuli Event). *Earth-Sci. Rev.* **127**, 242–261 (2013).
15. Priyatkina, N., Khudoley, A. K., Ustinov, V. N. & Kullerud, K. 1.92 Ga kimberlitic rocks from Kimozero, NW Russia: Their geochemistry, tectonic setting and unusual field occurrence. *Precambrian Res.* **249**, 162–179 (2014).
16. Stepanova, A., Samsonov, A. & Larionov, A. The final episode of middle Proterozoic magmatism in the Onega structure: Data on trans-Onega dolerites. *Trans. Karelian Res. Cent. Russ. Acad. Sci. Precambrian Geol. Ser.* **1**, 3–16 (2014).
17. Martin, A. P. *et al.* Multiple Palaeoproterozoic carbon burial episodes and excursions. *Earth Planet. Sci. Lett.* **424**, 226–236 (2015).

18. Puchtel, I. S. *et al.* Petrology of mafic lavas within the Onega plateau, central Karelia: evidence for 2.0 Ga plume-related continental crustal growth in the Baltic Shield. *Contrib. Mineral. Petrol.* **130**, 134–153 (1998).
19. Puchtel, I. S., Brügmann, G. E. & Hofmann, A. W. Precise Re–Os mineral isochron and Pb–Nd–Os isotope systematics of a mafic–ultramafic sill in the 2.0 Ga Onega plateau (Baltic Shield). *Earth Planet. Sci. Lett.* **170**, 447–461 (1999).
20. Breillat, N., Guerrot, C., Marcoux, E. & Négrel, Ph. A new global database of δ^{98}Mo in molybdenites: A literature review and new data. *J. Geochem. Explor.* **161**, 1–15 (2016).
21. Kendall, B., Dahl, T. W. & Anbar, A. D. The stable isotope geochemistry of molybdenum. *Rev. Mineral. Geochem.* **82**, 683–732 (2017).
22. Bell, K. G. Uranium and other trace elements in petroleums and rock asphalts. *Geol. Surv. Prof. Pap.* **356 B**, 44–65 (1960).
23. Ventura, G. T. *et al.* The stable isotope composition of vanadium, nickel, and molybdenum in crude oils. *Appl. Geochem.* **59**, 104–117 (2015).
24. Migdisov, A. A. *et al.* Hydrocarbons as ore fluids. *Geochem. Perspect. Lett.* **5**, 47–52 (2017).
25. Asael, D., Rouxel, O., Poulton, S. W., Lyons, T. W. & Bekker, A. Molybdenum record from black shales indicates oscillating atmospheric oxygen levels in the early Paleoproterozoic. *Am. J. Sci.* **318**, 275–299 (2018).
26. Paiste, K. Reconstructing the Paleoproterozoic sulfur cycle: Insights from the multiple sulfur isotope record of the Zaonega Formation, Karelia, Russia. PhD thesis, Univ. Tromsø (2018).

27. Miller, C. A., Peucker-Ehrenbrink, B., Walker, B. D. & Marcantonio, F. Re-assessing the surface cycling of molybdenum and rhenium. *Geochim. Cosmochim. Acta* **75**, 7146–7179 (2011).
28. Anderson, R. F., Fleisher, M. Q. & LeHuray, A. P. Concentration, oxidation state, and particulate flux of uranium in the Black Sea. *Geochim. Cosmochim. Acta* **53**, 2215–2224 (1989).
29. Partin, C. A. *et al.* Large-scale fluctuations in Precambrian atmospheric and oceanic oxygen levels from the record of U in shales. *Earth Planet. Sci. Lett.* **369–370**, 284–293 (2013).
30. Sheen, A. I. *et al.* A model for the oceanic mass balance of rhenium and implications for the extent of Proterozoic ocean anoxia. *Geochim. Cosmochim. Acta* **227**, 75–95 (2018).
31. Algeo, T. J. & Lyons, T. W. Mo–total organic carbon covariation in modern anoxic marine environments: Implications for analysis of paleoredox and paleohydrographic conditions. *Paleoceanography* **21**, PA1016 (2006).
32. Scott, C. *et al.* Tracing the stepwise oxygenation of the Proterozoic ocean. *Nature* **452**, 456–459 (2008).
33. Konhauser, K. O. *et al.* Aerobic bacterial pyrite oxidation and acid rock drainage during the Great Oxidation Event. *Nature* **478**, 369–373 (2011).
34. Reinhard, C. T. *et al.* Proterozoic ocean redox and biogeochemical stasis. *Proc. Natl. Acad. Sci. U. S. A.* **110**, 5357–5362 (2013).
35. Och, L. M. & Shields-Zhou, G. A. The Neoproterozoic oxygenation event: Environmental perturbations and biogeochemical cycling. *Earth-Sci. Rev.* **110**, 26–57 (2012).

36. Sahoo, S. K. *et al.* Ocean oxygenation in the wake of the Marinoan glaciation. *Nature* **489**, 546–549 (2012).
37. Morford, J. L. & Emerson, S. The geochemistry of redox sensitive trace metals in sediments. *Geochim. Cosmochim. Acta* **63**, 1735–1750 (1999).
38. Henderson, G. M. & Anderson, R. F. The U-series Toolbox for Paleoceanography. *Rev. Mineral. Geochem.* **52**, 493–531 (2003).
39. Helz, G. R. *et al.* Mechanism of molybdenum removal from the sea and its concentration in black shales: EXAFS evidence. *Geochim. Cosmochim. Acta* **60**, 3631–3642 (1996).
40. Andersen, M. B. *et al.* A modern framework for the interpretation of $^{238}U/^{235}U$ in studies of ancient ocean redox. *Earth Planet. Sci. Lett.* **400**, 184–194 (2014).
41. Föllmi, K. B. *et al.* Phosphogenesis and organic-carbon preservation in the Miocene Monterey Formation at Naples Beach, California - The Monterey hypothesis revisited. *Bull. Geol. Soc. Am.* **117**, 589–619 (2005).
42. Scholz, F. *et al.* Sedimentary molybdenum cycling in the aftermath of seawater inflow to the intermittently euxinic Gotland Deep, Central Baltic Sea. *Chem. Geol.* **491**, 27–38 (2018).
43. Morford, J. L., Emerson, S. R., Breckel, E. J. & Kim, S. H. Diagenesis of oxyanions (V, U, Re, and Mo) in pore waters and sediments from a continental margin. *Geochim. Cosmochim. Acta* **69**, 5021–5032 (2005).
44. Siebert, C., Nägler, T. F., von Blanckenburg, F. & Kramers, J. D. Molybdenum isotope records as a potential new proxy for paleoceanography. *Earth Planet. Sci. Lett.* **211**, 159–171 (2003).

45. Voegelin, A. R. *et al.* The impact of igneous bedrock weathering on the Mo isotopic composition of stream waters: Natural samples and laboratory experiments. *Geochim. Cosmochim. Acta* **86**, 150–165 (2012).
46. Barling, J., Arnold, G. L. & Anbar, A. D. Natural mass-dependent variations in the isotopic composition of molybdenum. *Earth Planet. Sci. Lett.* **193**, 447–457 (2001).
47. Arnold, G. L., Anbar, A. D., Barling, J. & Lyons, T. W. Molybdenum isotope evidence for widespread anoxia in mid-Proterozoic oceans. *Science* **304**, 87–90 (2004).
48. Neubert, N., Nägler, T. F. & Böttcher, M. E. Sulfidity controls molybdenum isotope fractionation into euxinic sediments: Evidence from the modern Black Sea. *Geology* **36**, 775–778 (2008).
49. Poulson, R. L., Siebert, C., McManus, J. & Berelson, W. M. Authigenic molybdenum isotope signatures in marine sediments. *Geology* **34**, 617–620 (2006).
50. Siebert, C., McManus, J., Bice, A., Poulson, R. & Berelson, W. M. Molybdenum isotope signatures in continental margin marine sediments. *Earth Planet. Sci. Lett.* **241**, 723–733 (2006).
51. Poulson Brucker, R. L., McManus, J., Severmann, S. & Berelson, W. M. Molybdenum behavior during early diagenesis: Insights from Mo isotopes. *Geochem. Geophys. Geosystems* **10**, Q06010 (2009).
52. Goldberg, T. *et al.* Controls on Mo isotope fractionations in a Mn-rich anoxic marine sediment, Gullmar Fjord, Sweden. *Chem. Geol.* **296–297**, 73–82 (2012).
53. Dickson, A. J., Cohen, A. S. & Coe, A. L. Continental margin molybdenum isotope signatures from the early Eocene. *Earth Planet. Sci. Lett.* **404**, 389–395 (2014).
54. Nakagawa, Y. *et al.* The molybdenum isotopic composition of the modern ocean. *Geochem. J.* **46**, 131–141 (2012).

55. Tossell, J. A. Calculating the partitioning of the isotopes of Mo between oxidic and sulfidic species in aqueous solution. *Geochim. Cosmochim. Acta* **69**, 2981–2993 (2005).
56. Nägler, T. F., Neubert, N., Böttcher, M. E., Dellwig, O. & Schnetger, B. Molybdenum isotope fractionation in pelagic euxinia: Evidence from the modern Black and Baltic Seas. *Chem. Geol.* **289**, 1–11 (2011).
57. Wagner, M., Chappaz, A. & Lyons, T. W. Molybdenum speciation and burial pathway in weakly sulfidic environments: Insights from XAFS. *Geochim. Cosmochim. Acta* **206**, 18–29 (2017).
58. Poulton, S. W. & Canfield, D. E. Development of a sequential extraction procedure for iron: implications for iron partitioning in continentally derived particulates. *Chem. Geol.* **214**, 209–221 (2005).
59. Poulton, S. W. & Canfield, D. E. Ferruginous conditions: A dominant feature of the ocean through Earth's history. *Elements* **7**, 107–112 (2011).
60. Slotznick, S. P., Eiler, J. M. & Fischer, W. W. The effects of metamorphism on iron mineralogy and the iron speciation redox proxy. *Geochim. Cosmochim. Acta* **224**, 96–115 (2018).
61. Asael, D. *et al.* Coupled molybdenum, iron and uranium stable isotopes as oceanic paleoredox proxies during the Paleoproterozoic Shunga Event. *Chem. Geol.* **362**, 193–210 (2013).
62. Crosby, C. H. & Bailey, J. V. The role of microbes in the formation of modern and ancient phosphatic mineral deposits. *Front. Microbiol.* **3**, 241 (2012).
63. Barnes, C. E. & Cochran, J. K. Uranium geochemistry in estuarine sediments: Controls on removal and release processes. *Geochim. Cosmochim. Acta* **57**, 555–569 (1993).

64. Kurzweil, F., Wille, M., Schoenberg, R., Taubald, H. & Van Kranendonk, M. J. Continuously increasing δ^{98}Mo values in Neoarchean black shales and iron formations from the Hamersley Basin. *Geochim. Cosmochim. Acta* **164**, 523–542 (2015).
65. Dickson, A. J. A molybdenum-isotope perspective on Phanerozoic deoxygenation events. *Nat. Geosci.* **10**, 721–726 (2017).
66. Lu, X. *et al.* Marine redox conditions during deposition of Late Ordovician and Early Silurian organic-rich mudrocks in the Siljan ring district, central Sweden. *Chem. Geol.* **457**, 75–94 (2017).
67. Partin, C. A., Bekker, A., Planavsky, N. J. & Lyons, T. W. Euxinic conditions recorded in the ca. 1.93 Ga Bravo Lake Formation, Nunavut (Canada): Implications for oceanic redox evolution. *Chem. Geol.* **417**, 148–162 (2015).
68. Weyer, S. *et al.* Natural fractionation of 238U/235U. *Geochim. Cosmochim. Acta* **72**, 345–359 (2008).
69. Tissot, F. L. H. & Dauphas, N. Uranium isotopic compositions of the crust and ocean: Age corrections, U budget and global extent of modern anoxia. *Geochim. Cosmochim. Acta* **167**, 113–143 (2015).
70. Ku, T.-L., Knauss, K. G. & Mathieu, G. G. Uranium in open ocean: concentration and isotopic composition. *Deep Sea Res.* **24**, 1005–1017 (1977).
71. Sarmiento, J. L. & Gruber, N. *Ocean Biogeochemical Dynamics*. (Princeton University Press, Princeton, 2006).
72. Dunk, R. M., Mills, R. A. & Jenkins, W. J. A reevaluation of the oceanic uranium budget for the Holocene. *Chem. Geol.* **190**, 45–67 (2002).
73. Andersen, M. B. *et al.* Closing in on the marine $^{238}U/^{235}U$ budget. *Chem. Geol.* **420**, 11–22 (2016).

74. Andersen, M. B., Stirling, C. H. & Weyer, S. Uranium Isotope Fractionation. *Rev. Mineral. Geochem.* **82**, 799–850 (2017).
75. Romaniello, S. J., Herrmann, A. D. & Anbar, A. D. Uranium concentrations and $^{238}U/^{235}U$ isotope ratios in modern carbonates from the Bahamas: Assessing a novel paleoredox proxy. *Chem. Geol.* **362**, 305–316 (2013).
76. Andersen, M. B. *et al.* The terrestrial uranium isotope cycle. *Nature* **517**, 356–359 (2015).
77. Noordmann, J., Weyer, S., Georg, R. B., Jöns, S. & Sharma, M. $^{238}U/^{235}U$ isotope ratios of crustal material, rivers and products of hydrothermal alteration: new insights on the oceanic U isotope mass balance. *Isotopes Environ. Health Stud.* **52**, 141–163 (2016).
78. Kendall, B., Brennecka, G. A., Weyer, S. & Anbar, A. D. Uranium isotope fractionation suggests oxidative uranium mobilization at 2.50Ga. *Chem. Geol.* **362**, 105–114 (2013).
79. Wang, X. *et al.* A Mesoarchean shift in uranium isotope systematics. *Geochim. Cosmochim. Acta* **238**, 438–452 (2018).
80. Gilleaudeau, G. J. *et al.* Uranium isotope evidence for limited euxinia in mid-Proterozoic oceans. *Earth Planet. Sci. Lett.* **521**, 150–157 (2019).
81. Yang, S., Kendall, B., Lu, X., Zhang, F. & Zheng, W. Uranium isotope compositions of mid-Proterozoic black shales: Evidence for an episode of increased ocean oxygenation at 1.36Ga and evaluation of the effect of post-depositional hydrothermal fluid flow. *Precambrian Res.* **298**, 187–201 (2017).
82. Kendall, B. *et al.* Uranium and molybdenum isotope evidence for an episode of widespread ocean oxygenation during the late Ediacaran Period. *Geochim. Cosmochim. Acta* **156**, 173–193 (2015).

83. Dahl, T. W. *et al.* Uranium isotopes distinguish two geochemically distinct stages during the later Cambrian SPICE event. *Earth Planet. Sci. Lett.* **401**, 313–326 (2014).

84. Abe, M., Suzuki, T., Fujii, Y., Hada, M. & Hirao, K. An ab initio molecular orbital study of the nuclear volume effects in uranium isotope fractionations. *J. Chem. Phys.* **129**, 164309 (2008).

85. Stirling, C. H., Andersen, M. B., Warthmann, R. & Halliday, A. N. Isotope fractionation of ^{238}U and ^{235}U during biologically-mediated uranium reduction. *Geochim. Cosmochim. Acta* **163**, 200–218 (2015).

86. Noordmann, J. *et al.* Uranium and molybdenum isotope systematics in modern euxinic basins: Case studies from the central Baltic Sea and the Kyllaren fjord (Norway). *Chem. Geol.* **396**, 182–195 (2015).

87. Rudnick, R. L. & Gao, S. Composition of the Continental Crust. in *Treatise on Geochemistry* 1–51 (Elsevier, Amsterdam 2014).

88. Karhu, J. A. Carbon isotopes. in *Encyclopedia of Geochemistry* (eds. Marshall, C. P. & Fairbridge, R. W.) 67–73 (Kluwer Academic Publishers, Boston, 1999).

89. Chappaz, A. *et al.* Does pyrite act as an important host for molybdenum in modern and ancient euxinic sediments? *Geochim. Cosmochim. Acta* **126**, 112–122 (2014).

90. Dahl, T. W. *et al.* Evidence of molybdenum association with particulate organic matter under sulfidic conditions. *Geobiology* **15**, 311–323 (2017).

91. Emerson, S. R. & Huested, S. S. Ocean anoxia and the concentrations of molybdenum and vanadium in seawater. *Mar. Chem.* **34**, 177–196 (1991).

92. Crusius, J., Calvert, S., Pedersen, T. & Sage, D. Rhenium and molybdenum enrichments in sediments as indicators of oxic, suboxic and sulfidic conditions of deposition. *Earth Planet. Sci. Lett.* **145**, 65–78 (1996).
93. Algeo, T. J. & Tribovillard, N. Environmental analysis of paleoceanographic systems based on molybdenum–uranium covariation. *Chem. Geol.* **268**, 211–225 (2009).
94. Taylor, A. P., Barry, J. C. & Webb, R. I. Structural and morphological anomalies in magnetosomes: possible biogenic origin for magnetite in ALH84001. *J. Microsc.* **201**, 84–106 (2001).
95. Strauss, H. *et al.* Enhanced accumulation of organic matter: The Shunga Event. in *Reading the Archive of Earth's Oxygenation* (eds. Melezhik, V. A. et al.) vol. 3: Global Events and the Fennoscandian Arctic Russia-Drilling Earth Project 1195–1273 (Springer, Berlin Heidelberg, 2013).
96. Konhauser, K. O. *et al.* Iron formations: A global record of Neoarchaean to Palaeoproterozoic environmental history. *Earth-Sci. Rev.* **172**, 140–177 (2017).
97. Isley, A. E. & Abbott, D. H. Plume-related mafic volcanism and the deposition of banded iron formation. *J. Geophys. Res. Solid Earth* **104**, 15461–15477 (1999).
98. Holland, H. D. *The Chemical Evolution of the Atmosphere and Oceans*. (Princeton University Press, 1984).
99. Canfield, D. E. A new model for Proterozoic ocean chemistry. *Nature* **396**, 450–453 (1998).
100. Planavsky, N. J., Bekker, A., Hofmann, A., Owens, J. D. & Lyons, T. W. Sulfur record of rising and falling marine oxygen and sulfate levels during the Lomagundi event. *Proc. Natl. Acad. Sci. U. S. A.* **109**, 18300–18305 (2012).

101. Scott, C. *et al.* Pyrite multiple-sulfur isotope evidence for rapid expansion and contraction of the early Paleoproterozoic seawater sulfate reservoir. *Earth Planet. Sci. Lett.* **389**, 95–104 (2014).

102. Kipp, M. A., Stüeken, E. E., Bekker, A. & Buick, R. Selenium isotopes record extensive marine suboxia during the Great Oxidation Event. *Proc. Natl. Acad. Sci. U. S. A.* **114**, 875–880 (2017).

103. Bekker, A. & Holland, H. D. Oxygen overshoot and recovery during the early Paleoproterozoic. *Earth Planet. Sci. Lett.* **317–318**, 295–304 (2012).

104. Canfield, D. E. *et al.* Oxygen dynamics in the aftermath of the Great Oxidation of Earth's atmosphere. *Proc. Natl. Acad. Sci. U. S. A.* **110**, 16736–16741 (2013).

105. Zbinden, E. A., Holland, H. D., Feakes, C. R. & Dobos, S. K. The sturgeon falls paleosol and the composition of the atmosphere 1.1 Ga BP. *Precambrian Res.* **42**, 141–163 (1988).

106. Planavsky, N. J. *et al.* Low Mid-Proterozoic atmospheric oxygen levels and the delayed rise of animals. *Science* **346**, 635–638 (2014).

107. Tang, D., Shi, X., Wang, X. & Jiang, G. Extremely low oxygen concentration in mid-Proterozoic shallow seawaters. *Precambrian Res.* **276**, 145–157 (2016).

108. Bellefroid, E. J. *et al.* Constraints on Paleoproterozoic atmospheric oxygen levels. *Proc. Natl. Acad. Sci. U. S. A.* **115**, 8104–8109 (2018).

109. Siebert, C., Nägler, T. F. & Kramers, J. D. Determination of molybdenum isotope fractionation by double-spike multicollector inductively coupled plasma mass spectrometry. *Geochem. Geophys. Geosystems* **2**, 1032 (2001).

110. Nägler, T. F. *et al.* Proposal for an international molybdenum isotope measurement standard and data representation. *Geostand. Geoanal. Res.* **38**, 149–151 (2014).

111. Goldberg, T. *et al.* Resolution of inter-laboratory discrepancies in Mo isotope data: an intercalibration. *J. Anal. At. Spectrom.* **28**, 724–735 (2013).

112. Zhang, F. *et al.* Global marine redox changes drove the rise and fall of the Ediacara biota. *Geobiology* **17**, 594–610 (2019).

113. Zhang, F. *et al.* Extensive marine anoxia during the terminal Ediacaran Period. *Sci. Adv.* **4**, eaan8983 (2018).

114. Zhang, F. *et al.* Multiple episodes of extensive marine anoxia linked to global warming and continental weathering following the latest Permian mass extinction. *Sci. Adv.* **4**, e1602921 (2018).